Electrochimica Acta 541 (2025) 147365

Contents lists available at ScienceDirect

Electrochimica Acta

journal homepage: www.journals.elsevier.com/electrochimica-acta

Development of a sustainable *g*-C_3N_4/CNT composite sensor for nicotine analysis in e-cigarette liquids

Reshma Nair [a], Danielson Ngo Joseph [c], Francesco Spiedo [a], Bal Virdee [b], Bhaven Patel [a], Devagi Kanakaraju [c], Priyanka Ganguly [a,*]

[a] Applied Chemistry & Pharmaceutical Technology (ADAPT), School of Human Sciences, London Metropolitan University, London N7 8DB, UK
[b] Center for Communications Technology, School of Computing and Digital Media, London Metropolitan University, 166-220 Holloway Road, London, N7 8DB, UK
[c] Chemistry Programme, Faculty of Resource Science and Technology, Universiti Malaysia Sarawak, 94300 Kota Samarahan, Sarawak, Malaysia

ARTICLE INFO

Keywords:
Disposable sensor
Nicotine
Printed sensor
Vapes

ABSTRACT

The accurate quantification of nicotine in e-cigarette liquids is critical due to its potent physiological effects and potential for misuse. In this study, we report the development of a sustainable electrochemical sensor based on a composite of graphitic carbon nitride (*g*-C_3N_4) and multiwalled carbon nanotubes (CNTs) for the sensitive detection of nicotine. The *g*-C_3N_4/CNT nanocomposite was immobilised onto a glassy carbon electrode (GCE) using chitosan as a biocompatible and adhesive matrix. CNTs were employed to overcome the inherent low conductivity of *g*-C_3N_4, while chitosan ensured mechanical stability of the modified electrode. SEM-EDX analysis reveals *g*-C_3N_4 nanosheets interwoven with tube-like CNTs networks, with no foreign elements detected, suggesting the formation of a highly pure nanocomposite. Electrochemical characterisation revealed high selectivity and sensitivity toward nicotine under neutral pH conditions, achieving a detection limit of 0.0773 mM and a limit of quantification of 0.2343 mM. The sensor also exhibited excellent repeatability and operational stability at room temperature. The carbon based printed modified sensor also displayed similar results. Application to commercial vape samples demonstrated the practical utility of the method, with results showing strong agreement with high performance liquid chromatography (HPLC) analysis. This work highlights the promise of *g*-C_3N_4/CNT composites as green and effective sensing materials for nicotine monitoring in consumer products.

1. Introduction

Vaping culture has surged in popularity over the last decade, presenting a popular, fancy alternative to traditional smoking, which is considered less toxic [1]. Vape, commonly referred to as an e-cigarette, is an electronic device that vaporises the e-liquid using a battery powered coil, producing an aerosol that users inhale, delivering nicotine into the lungs without combustion [2]. E-liquids typically contain nicotine, propylene glycol, vegetable glycerine, and flavourings [3]. Nicotine, a toxic, parasympathomimetic stimulant and highly addictive metabolite found in tobacco leaves, is commonly present in concentrations of approximately 1–3 % in tobacco products. The chemical structure of nicotine is represented as 3-(1-methylpyrrolidin-2-yl) pyridine ($C_{10}H_{14}N_2$), shown in Scheme 1, and it constitutes about 2–8 % of the *Nicotiana genus* (tobacco plants), such as *N. Rustica* and *N. Tabacum* [4, 5]. This oily, hygroscopic liquid is colourless to pale yellow and is soluble in water at room temperature. Nicotine can be rapidly absorbed directly into the human body and affects the nervous system. Regular intake can lead to serious health issues, including increased blood pressure, heart rate, and various cancers, while also having potential therapeutic effects for conditions like Alzheimer's and Parkinson's diseases [6]. Over time, users can develop a tolerance, prompting them to consume higher amounts and seek products with greater nicotine concentrations. This growing demand has fuelled the black markets, where illegally imported or unregulated vapes often contain nicotine levels that surpass legal limits. Such products pose significant health risks, and numerous reports worldwide have highlighted this concerning trend. Despite legal restrictions in the UK prohibiting the sale of vaping products to individuals under 18 and limiting nicotine content to a maximum of 20 mg/mL, the demand for higher nicotine levels persists [7–10].

The increased use of vapes among school-going youth is often driven by the misconception that vaping is a healthy alternative to cigarettes, along with the appeal of sweet flavours like fruits, bubble gum and

* Corresponding author.
E-mail address: p.ganguly@londonmet.ac.uk (P. Ganguly).

https://doi.org/10.1016/j.electacta.2025.147365
Received 23 June 2025; Received in revised form 28 August 2025; Accepted 9 September 2025
Available online 11 September 2025

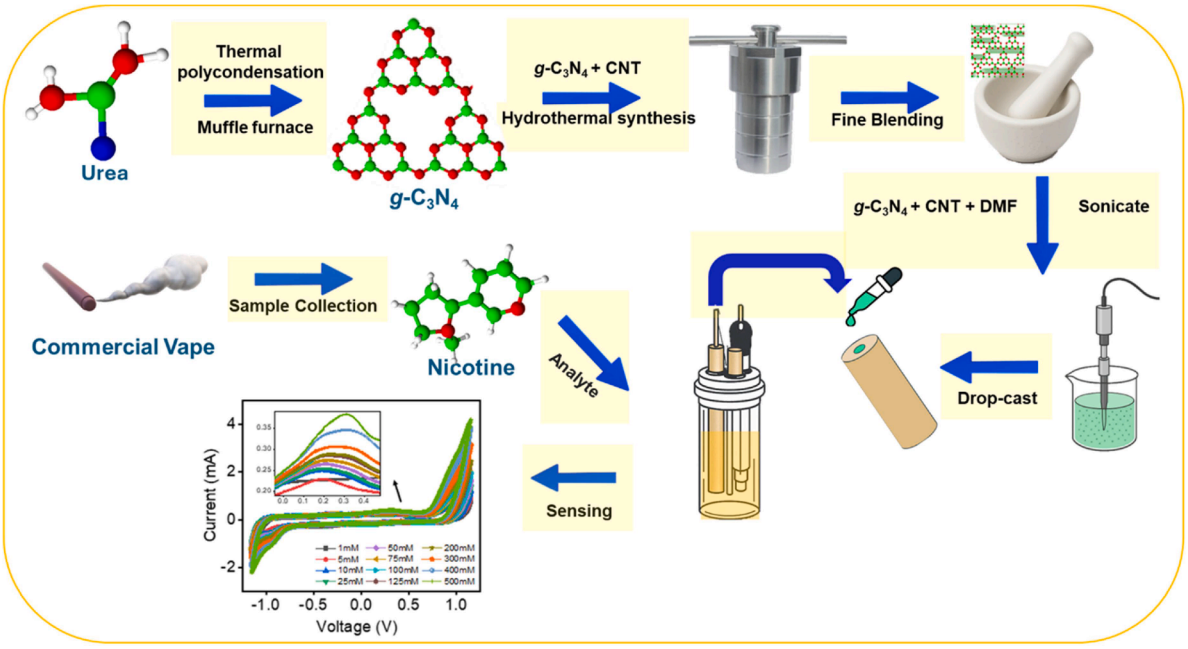

Scheme 1. Overview of the synthesis and modification process of GCE.

candy [9]. Given the health implications, there is a growing need for effective nicotine detection methods in toxicology, the tobacco industry, and medical research [4,11]. Traditional analytical techniques such as gas chromatography-mass spectrometry (GC–MS) [12,13], spectrofluorimetric [14], high-performance liquid chromatography (HPLC) [15–17], spectrophotometry [18], radioimmunoassays [19,20], amperometric assays [21], electrochemiluminescence (ECL) [22], liquid chromatography-mass spectrometry (LC-MS) [23], and capillary electrophoresis [24] have been widely used but often involve high costs, complex sample extraction and preparation processes. As a solution, researchers have developed alternative electrochemical sensors that offer a more convenient and cost-effective alternative for nicotine detection. Recent advances in electrochemical sensors for nicotine detection have focused on enhancing surface properties and employing novel composite materials to achieve lower detection limits and broader linear ranges. Boron-doped diamond electrodes (BDDE) operated *via* differential pulse voltammetry (DPV) in ammonium buffer (pH 7.5) achieved a detection limit of 0.01 mg L^{-1} across 0.03–0.40 mg L^{-1}, offering a robust platform for e-liquid nicotine monitoring [25]. $CuWO_4$/reduced graphene oxide/Nafion-modified GCE further lowered the detection limit to 0.005 mg L^{-1} over a 0.02–0.14 mg L^{-1} range, enabling practical analysis of both cigarette and urine samples with exceptional sensitivity [26]. Low-cost, disposable sensors based on 3D-printed polylactic acid/carbon black (PLA/CB) electrodes have also emerged, albeit with higher limits (2.7 mg L^{-1}, range 6.5–81 mg L^{-1}), suitable for sweat and e-liquid assays [27]. Most recently, a tadpole-like gold nanostructure immobilised on titanium oxide (Au–TiO_2) employed SWV at pH 7.0 achieved an LOD of 0.149 µmol L^{-1} and LOQ 0.497 µmol L^{-1} [28].

2D nanomaterials, such as graphitic carbon nitride (*g*-C_3N_4), could be utilised as a potential material for developing sustainable electrochemical devices [29]. *g*-C_3N_4 is a metal-free polymeric semiconductor with a layered 2D structure analogous to graphene, where weak van der Waals forces hold layers together [30]. Its structure contains nitrogen bridges, introducing defects and active sites that enhance chemical reactivity. *g*-C_3N_4 has gained significant attention among researchers due to its visible-light photocatalytic activity, high thermal and chemical stability, tuneable electronic properties, low production cost, and abundant availability [31,32]. Its conjugated structure facilitates rapid electron transfer, biocompatibility, and catalytic behaviour, further expanding its application potential. These distinctive features make *g*-C_3N_4 a highly versatile material for emerging technologies, particularly in photocatalysis, energy storage and conversion, chemical sensing, drug delivery, and environmental remediation. It's simple and scalable synthesis enhances its feasibility for industrial scale production [33,34].

g-C_3N_4 has been utilised as an effective modifier in electrochemical detection systems, due to its ability to amplify signal responses. It exhibits selective interactions with target molecules, stabilises the analyte, and minimises background noise. Its nitrogen-rich framework, natural abundance, high electronic conductivity, and excellent physicochemical and electrochemical stability make it a promising candidate as an electrode material or a surface modifier [35]. The 2D form of *g*-C_3N_4 exhibits impressive electrochemical properties, including high capacity, substantial energy density, and long cycle life, making it ideal for probing electrochemical behaviours. Its unique surface properties such as excellent adsorption capability, biocompatibility, low toxicity, large surface-to-volume ratio, superparamagnetic characteristics, and strong electrocatalytic activity make *g*-C_3N_4 a valuable addition for electrode modifications [36]. Carbon-printed electrodes (CPE) were utilised with an Anapot for real-time vape sample testing. The geometry of the SPE consists of a reference electrode (RE) made of silver/silver chloride, a working electrode (WE) and a counter electrode (CE), both made of carbon, and a substrate (SUB) made of polyethylene terephthalate (PET). These electrodes are popular because they are suitable for disposable applications due to their biocompatibility and ease of modification[37,38]. Their compact size and user-friendly design facilitate continuous monitoring in non-laboratory settings, and they are cost-effective too [35].

This work presents a novel, sustainable composite of *g*-C_3N_4/CNT, designed to develop a sensor material for nicotine detection. The identification of nicotine in commercial vape samples is intrinsic and time consuming when using traditional methods. To overcome this, the sensor has been developed, and the results are discussed below.

- The surface of the GCE is modified by a novel composite of *g*-C_3N_4 nanoparticles incorporated with multiwalled carbon nanotubes (CNTs) (90:10) with DMF as the solvent and chitosan as the binder.
- CNTs are used to address the low conductivity of *g*-C_3N_4, while chitosan serves as a binder to firmly attach the *g*-C_3N_4/CNT composite

onto the GCE without peeling off during testing. Both materials are biocompatible and low toxicity, making them sustainable.
- The resulting sensor demonstrates excellent selectivity, remarkable stability, a low detection limit (0.0773 mM), a limit of quantification (0.2343 mM), and good repeatability at room temperature.
- The sensor enables effective analysis of nicotine in commercial vape samples and identifies one of the tested commercial vape samples as having high nicotine content; the results were validated by the conventional HPLC method.
- The *g*-C_3N_4/CNT composite was further modified on the surface of a carbon-based printed electrode and tested using a portable potentiostat for real-time applications. The modified electrode shows notable stability, a low detection limit (0.0735 mM), a Limit of Quantification (0.2229 mM), and good repeatability at room temperature.

2. Experimental

2.1. Chemicals and reagents

Urea, *N, N*-dimethylformamide (DMF), chitosan (medium molecular weight), nicotine (≥99 %), multiwalled carbon nanotubes (L/D ~ 1000, ≥99.9 wt), phosphate buffered saline tablet (PBS), sodium hydroxide (NaOH), acetic acid (CH_3COOH) and hydrochloric acid (HCl) was purchased from Sigma-Aldrich. Double-deionised water (Suez) was used to prepare the nicotine stock solution and stored in dark conditions. Commercially available vapes were purchased from local shops and used directly for the preparation and analysis of real samples.

2.2. Characterisation

The surface morphology and elemental composition of the synthesised *g*-C_3N_4/CNT were characterised using a Scanning Electron Microscope (SEM) coupled with an Energy-Dispersive X-ray Spectroscopy (EDX) detector (model: JEOL-JSM IT500). Before the analysis, composite samples were uniformly dispersed onto a carbon tape affixed to an aluminium stub. Samples were then sputter-coated with a thin layer of gold (Au) under vacuum with a sputter coater. SEM imaging was carried out under vacuum conditions at an accelerating voltage of 10 kV. The crystalline structure and phase composition were investigated using X-ray Diffraction (XRD) analysis. Measurements were done using Cu Kα radiation ($\lambda = 0.154$ nm) in the scanning range of 2θ between 10° and 80°, with a scanning rate of 0.04 per second. The accelerating voltage and applied current that were used for this analysis were 45 kV and 40 mA, respectively. Phase identification was done by matching analysed data to an automatic Joint Committee on Powder Diffraction Standards (JCPDS) library search.

The electrochemical workstation used to investigate the sensor's performance using Biologic SP-50e potentiostat. The sample's pH variations are measured using a multi-function digital pH meter, and the sonicator used is from Richmond Scientific Ltd. The Anapot and 501 carbon-printed electrodes were purchased from Zimmer and Peacock. HPLC analysis was performed using the Agilent Technologies 1260 Infinity II.

2.3. Synthesis of g-C_3N_4

g-C_3N_4 was synthesised using thermal polycondensation with urea as the precursor [30]. 10 g of finely powdered urea, prepared to ensure uniform particle size, was placed in a porcelain crucible and loosely covered to allow gaseous byproducts to escape while minimising contamination. The crucible was heated in a muffle furnace at a controlled ramp rate of 3 °C/min up to 550 °C under an air atmosphere. The temperature was maintained at 550 °C for 2 h to allow condensation reactions to occur, forming *g*-C_3N_4 while releasing gaseous byproducts. During the process, urea ($CO(NH_2)_2$) thermally decomposes and undergoes condensation reactions, forming *g*-C_3N_4 and releasing ammonia (NH_3) and carbon dioxide (CO_2) as byproducts. After the reaction, the muffle furnace was allowed to cool naturally to room temperature to prevent structural damage to the product. A yellow to light brown powder obtained after cooling was visually identified as graphitic carbon nitride (*g*-C_3N_4).

2.4. Modification of g-C_3N_4 with CNT

The composite was prepared *via* hydrothermal synthesis. Prepared *g*-C_3N_4 powder was dispersed into a CNT suspension at a 90:10 wt ratio (*g*-C_3N_4: CNT). The CNTs were suspended in an acidified (H_2SO_4) aqueous solution containing Triton X-100 as a surfactant, and the mixture was uniformly dispersed by ultrasonication. The resulting *g*-C_3N_4/CNT mixture was transferred to a Teflon-lined autoclave and subjected to hydrothermal treatment at 180 °C for 6 h. After synthesis, the composite was washed thoroughly with deionised water and ethanol and dried at 60 °C for 12 h. The dried powder was gently ground with a pestle and mortar and dissolved in 5 mL of DMF. Finally, the suspension was sonicated for a total of 1 h, in 10 min intervals, to ensure complete dispersion.

2.5. Preparation of g-C_3N_4/CNT/GCE based sensor

The GCE was thoroughly cleaned and polished using a GCE polishing kit, sonicated for 5 min, washed with deionised water, and air-dried. The drop casting technique was used to deposit the compound onto the GCE, which has a diameter of 3 mm. A 5 μL of targeted material was drop cast each time and dried in an oven at 70 °C for 15 min, repeated four times. Afterwards, 5 μL of 2 % chitosan dissolved in acetic acid was drop-cast on top and dried for 15 min in an oven at 70 °C. Scheme 1 displays a summarised glance of the synthesis and the modification of the GCE.

2.6. Preparation of printed electrode

The drop casting technique was employed to deposit the *g*-C_3N_4/CNT onto the printed electrode. A 2 μL aliquot of the *g*-C_3N_4/CNT was drop cast each time and dried in an oven at 70 °C for 15 min, with this process repeated three times. Following this, 2 μL of a 2 % chitosan solution dissolved in acetic acid was drop-cast on top and dried for 15 min at 70 °C.

2.7. Electrochemical characterisation

The electrochemical experiments were conducted using a three-electrode configuration. The working electrodes used in the study are different modifications of GCE with *g*-C_3N_4/CNT. The potentiostat controlled the working electrode's potential relative to the reference electrode (Ag/AgCl), while the counter electrode (Pt) completed the circuit, allowing precise control of the measurements. Electrochemical characterisation, cyclic voltammetry (CV), electrochemical impedance spectroscopy (EIS), and differential pulse voltammetry (DPV) were performed using an electrochemical workstation (Biologic SP-50e). CV measurements were recorded at scan rates ranging from 10 to 1000 mVs^{-1}. EIS spectra were collected over a frequency range of 10 Hz to 1 MHz for calibration and concentration studies, potentials from −1.15 V to 1.15 V were applied; for all other measurements, the potential window was −0.8 V to 0.8 V. All experiments were conducted at pH 7 and at room temperature.

2.8. pH study methods

The pH effect was evaluated from 2 to 9 using a 100 mM nicotine concentration in 0.1 M PBS solution. The original pH of the sample was 9.8 before adjustment. pH corrections were made with 6 M HCl and 2 M NaOH in the three-electrode system.

Table 1
Tabulated Detailed Information on Commercial Vape Samples used.

Company name	Flavour	Nicotine percentage	Batch number	Expiry Date	Nicotine dose per puff
Random tornado	Blueberry cherry cranberry	20 mg/ml, 2 %	—	—	66 µg
Elux legends	Grape	20 mg/ml, 2 %	KA20240315NJ	07/04/2026	133 µg
Ske crystal	Triple mango	10 mg/ml, 1 %	CRYTM 10–003	31/01/2027	110 µg
Hayati pro max	Triple mango	0 %	37EA23C	23/10/2026	0 µg

2.9. Validation

Analyses were conducted using a C18 Thermo analytical column (4.6 × 250 mm, 5 µm). The mobile phase consisted of 0.1 % triethylamine in ultrapure water and acetonitrile in a 70:30 ratio (v/v), under isocratic conditions at room temperature, with a flow rate of 1.0 mL/min. Nicotine UV absorbance was detected in the 210–400 nm range, while quantification was performed explicitly at 260 nm. A calibration curve was generated using five nicotine standard solutions at concentrations of 0.1, 0.5, 1, 5, and 7.5 mM. All prepared solutions were filtered through 0.22 µm syringe filters before injecting 10 µL into the HPLC system. To analyse vape samples, 0.5 mL of each sample with a 20-dilution factor was taken and filtered using 0.22 µm syringe filters, and 10 µL of each was injected for analysis.

2.10. Real sample analysis

Commercial vape samples were obtained from various local shops across London. Table 1 lists detailed information for the four samples tested. All vape samples were analysed at pH 7, adjusted using 6 M HCl and 2 M NaOH.

3. Results and discussion

3.1. Material characterisation

To confirm the formation of the polymeric tri-s-triazine structure of *g*-C_3N_4 in the synthesised sample, Fourier-Transform Infrared Spectroscopy (FTIR) was used (Fig. 1(a)). Peaks at 693.3 cm^{-1} and 760.4 cm^{-1} correspond to the out of plane bending and ring breathing modes of the triazine or heptazine units, representing heterocyclic frameworks [35]. The stretch at 1125.7 cm^{-1} arises from the C–N bridging nitrogen atoms, while the band at 1312 cm^{-1} reflects in-plane C–N vibrations. Stronger stretches at 1394.0 cm^{-1}, 1453.7 cm^{-1}, 1539.4 cm^{-1}, and 1625.1 cm^{-1} are associated with $C = N$ and C–N stretching vibrations within the conjugated aromatic structure, confirming the nitrogen-rich layered backbone [39]. The broad stretch at 3071.3 cm^{-1} corresponds to N–H stretching, suggesting the presence of terminal amine groups or adsorbed moisture. The observed bands related to the triazine/heptazine based aromatic framework, along with the C–N and $C = N$ stretching and bending modes, validate the successful formation of polymeric *g*-C_3N_4.

Further analysis *via* SEM for the synthesised *g*-C_3N_4/CNT was done to investigate the effect of varying the composition of *g*-C_3N_4 and CNT on the surface morphology of the samples, showed in supporting information **Fig. S1**. Additionally, chitosan, which was used as a binder, was also analysed as a blank sample. SEM micrograph shows the formation of smooth aggregates from the dissolution of chitosan in acetic acid

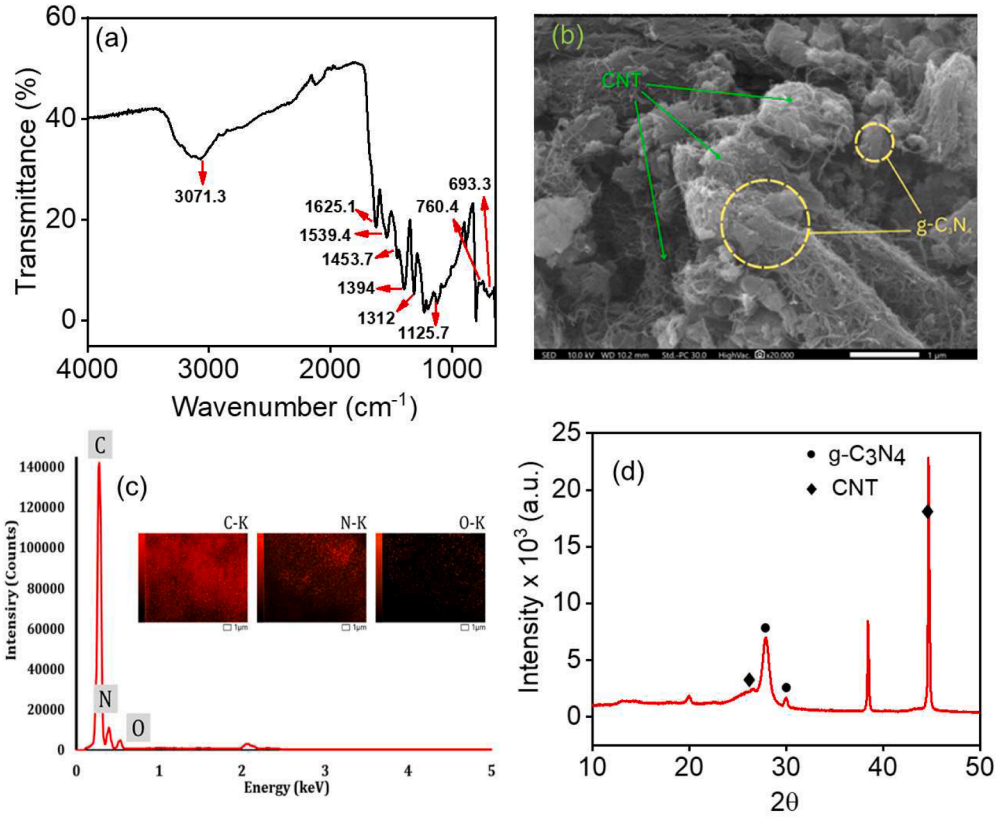

Fig. 1. (a) FTIR analysis of synthesised *g*-C_3N_4. (b) SEM micrograph of *g*-C_3N_4/CNT (90:10). (c) EDX and elemental mapping of *g*-C_3N_4/CNT. (d) XRD pattern of *g*-C_3N_4/CNT.

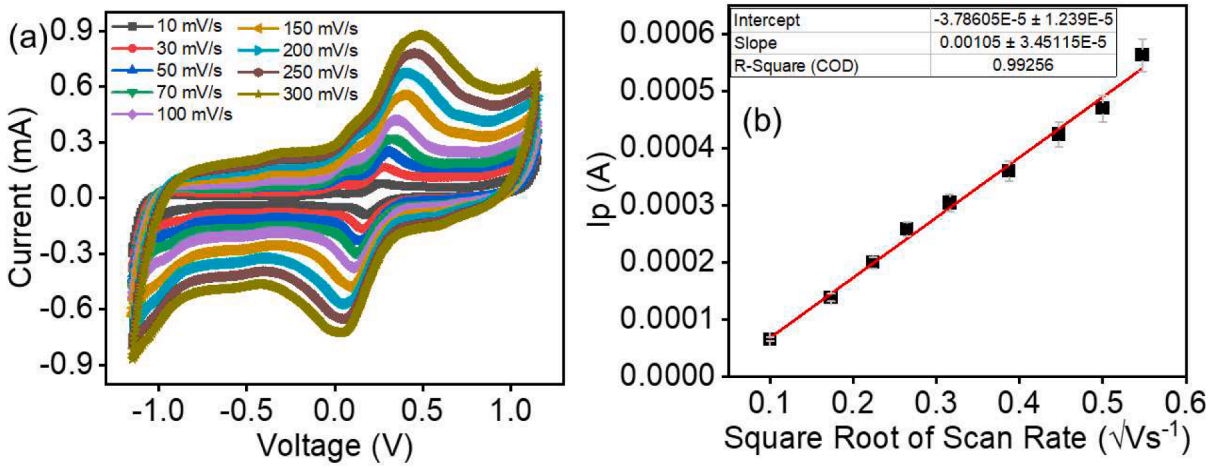

Fig. 2. (a) CV response of 5 mM $K_3[Fe(CN)_6$ in 0.1 M KCl scan rate ranging from 10 to 300 mV s^{-1} using g-C_3N_4/CNT-coated GCE, (b) Plot of I_P(A) *vs.* $\sqrt{\nu}$ ($\sqrt{Vs^{-1}}$).

(Fig. S1(a)). A previous study by Lukman et al. mentioned that the formation of chitosan with a smoother surface is desirable, especially in sensing applications, due to the enhanced surface properties [40]. Notably, the surface morphology of the *g*-C_3N_4/CNT for each composition shows slight variation. It was observed that when the composition of CNT was increased from 5 % to 15 %, more noticeable CNT tube-like networks were seen to be enveloped around the *g*-C_3N_4 layers, as shown in Fig. 1(b), **S1(b) and S1(c).** Increasing CNT composition also results in the formation of more closely packed *g*-C_3N_4 sheets. As seen in Fig. 1(b), *g*-C_3N_4 nanosheets are more closely packed with each other as the formation of a dense interwoven network of CNTs binds them together, altering the surface architecture. In contrast to the 5 % CNT composition in **Fig. S1(c)**, the *g*-C_3N_4 nanosheets are less packed. Moreover, EDX analysis shows the presence of carbon (C), nitrogen (N) and oxygen (O), which matches the expected composition of *g*-C_3N_4/CNT (Fig. 1(c)).

Additionally, phase identification of the synthesised *g*-C_3N_4/CNT was done *via* XRD **(Fig. S2)**. For sample *g*-C_3N_4/CNT (95:5) peaks at $2\theta = 27.9^\circ$ correspond to (002) lattice plane for hexagonal *g*-C_3N_4. However, no obvious peaks for CNT were detected likely due to the low content of CNT in the composite matrix. However, as CNT content increased to 10 % (Fig. 1(d)) and 15 %, *g*-C_3N_4 was found to have a hexagonal crystal system with space group P31C with diffraction peaks at $2\theta = 27.5^\circ$ and 38.3° (JCPDS 01–087–1522). Consequently, with the increase of CNT content, an overlapping peak of CNT at $2\theta = 26.0^\circ$ and strong peaks at

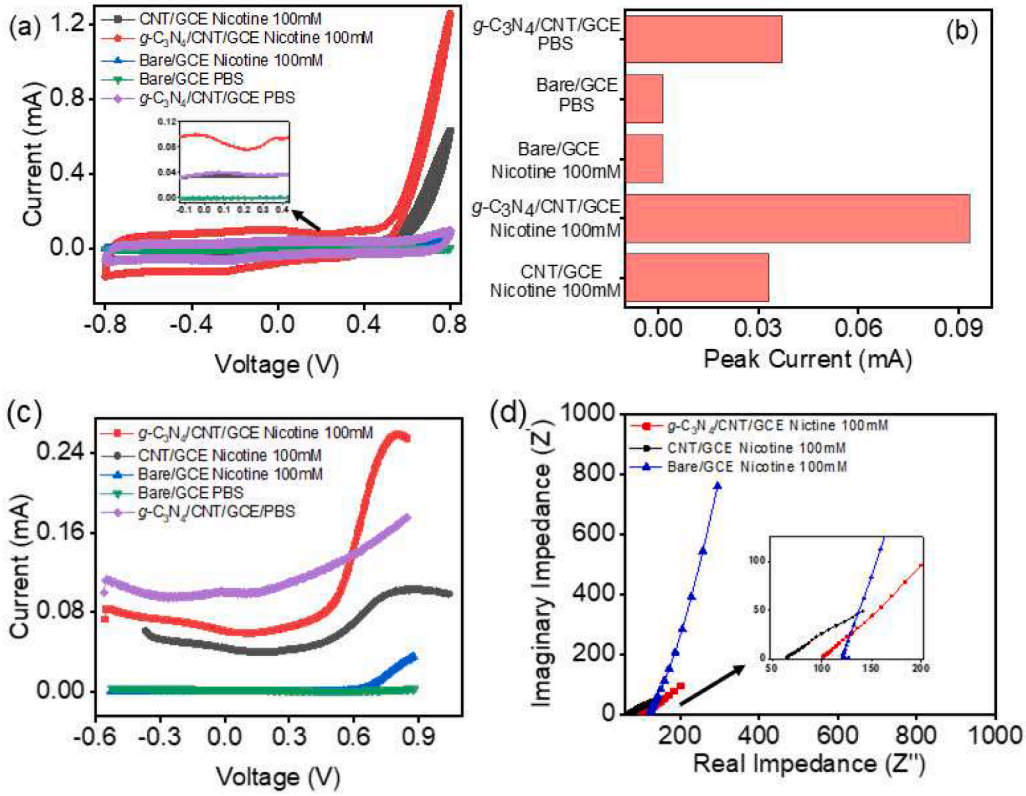

Fig. 3. Voltametric response in 0.1 M PBS (pH 7) with and without 100 mM **n**icotine on Bare GCE, CNT/GCE, and *g*-C_3N_4/CNT/GCE, (a) CV at a scan rate of 10 mVs^{-1} from –0.8 to 0.8 V. (b) Comparison of obtained peak current from CV. (c) DPV from 0 to 0.8 V with a pulse amplitude of 50 mV, pulse width of 250 ms, and a step potential of 5 mV. (d) Nyquist plot for 100 mM nicotine on bare GCE, CNT/GCE, and *g*-C_3N_4/CNT/GCE.

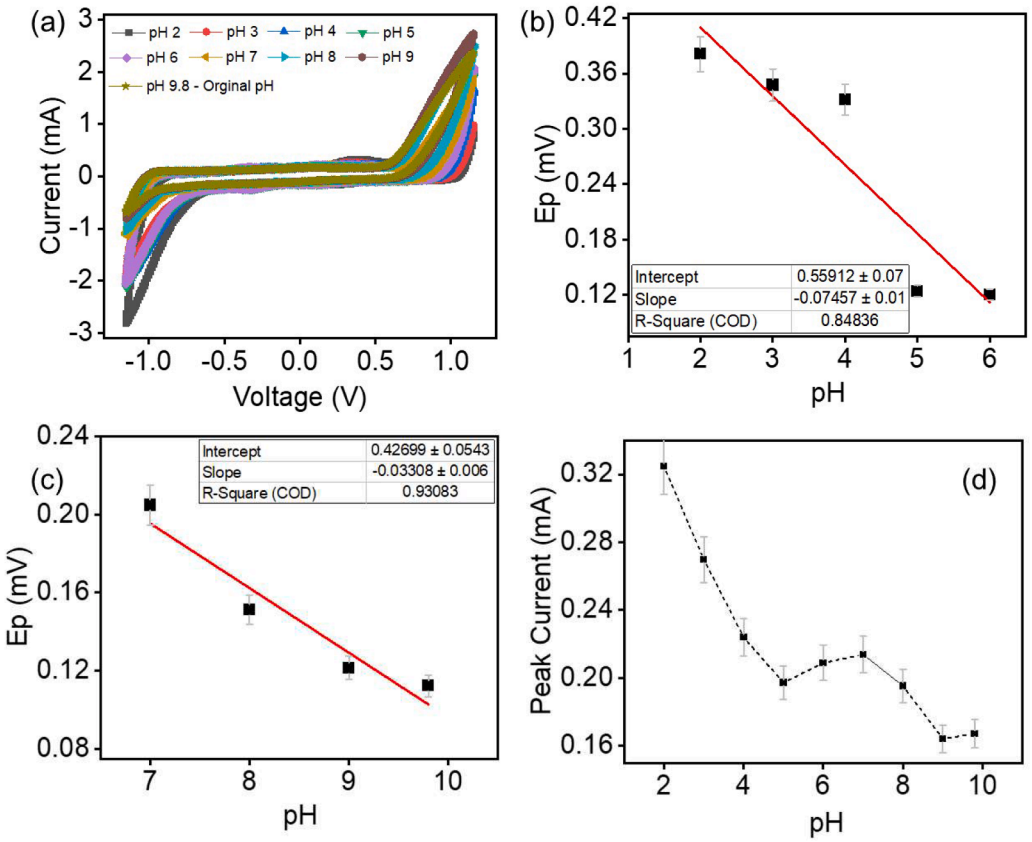

Fig. 4. (a) CV of *g*-C_3N_4/CNT/GCE in 100 mM nicotine in 0.1 M PBS at 50 mVs^{-1}, from −1.15 V to 1.15 V across a pH range of 2 to 9. (b) Relationship between Peak Potential (E_P) and acidic pH (2–6). (c) Relationship between Peak Potential (E_P) and neutral and alkaline pH (7–9). (d) Plot of Peak Current (I_P) *vs* pH.

$2\theta = 44.2^\circ$ correspond to (002) and (100) crystal planes for hexagonal CNT. This data confirms the successful integration of *g*-C_3N_4 and CNTs with a well-defined nanocomposite structure, suggesting strong interfacial interactions between the two components.

3.2. Electrochemical performance and surface area of g-C_3N_4/CNT

The active surface area of the prepared electrode was measured using CV, ranging from 10 to 300 mV s^{-1} (Fig. 2(a)). 5 mM potassium ferricyanide ($K_3[Fe(CN)_6]$) in 0.1 M potassium chloride (KCl) was used as the test solution because of its well-known redox properties and low toxicity [35,41,42]. The comparison of CVs at a scan rate of 50 mV s^{-1} showed that the g-C_3N_4/CNT-coated GCE had a much larger active surface area than the bare GCE **(Fig. S3(a))**. This increase in surface area is essential, as it provides more contact points between the electrode and the electrolyte, thereby improving the electrode's performance and sensitivity. To study this further, the Randles–Ševčík equation (Eq. (1)) was used to calculate the active surface areas.

$$I_p = \left(2.9 \times 10^5\right) n^{3/2} A^0 {D_R}^{1/2} \nu^{1/2} C_0 \quad (1)$$

Where n is the number of electrons, A is the surface area, D_R is the diffusion coefficient, ν is the scan rate, and C_0 is the concentration of $K_3[Fe(CN)_6]$ [35]. The modified GCE was found to have a surface area of 0.28 cm^2, while the unmodified GCE showed only around 0.05 cm^2. This confirms that adding g-C_3N_4/CNT greatly improves the electrochemical properties of the electrode. This is further supported by the Nyquist plot shown in **Fig. S3(b)**, where the impedance window of the GCE is higher. However, when coated with g-C_3N_4/CNT, the impedance is significantly reduced, which is good for electrochemical activities.

3.3. Electrochemical detection of nicotine

To analyse the electrocatalytic performance of *g*-C_3N_4/CNT/GCE in sensing 100 mM nicotine in 0.1 M PBS (pH 7) and just PBS, the electrode was prepared and tested at room temperature. This study aimed to understand the kinetics and performance of the modified electrode compared to other electrodes. Comparative analyses were conducted using CV and DPV at a scan rate of 10 mVs^{-1} from –0.8 to 0.8 V on bare GCE, bare GCE in PBS, CNT-modified GCE, *g*-C_3N_4-modified GCE, and *g*-C_3N_4/CNT-modified GCE, as shown in Fig. 3.

While analysing the CV graphs (Fig. 3(a)), both the bare GCE in nicotine and PBS exhibited a baseline response, and the *g*-C_3N_4/CNT/GCE in PBS was also close to the baseline. Although CNT showed enhanced performance due to its high surface area and electrical conductivity, it did not exhibit an anodic peak, indicating a lack of intense interaction with the targeted analyte, nicotine (Fig. 3(b)). The *g*-C_3N_4/CNT/GCE exhibited the highest anodic peak current, indicating better electron transfer and higher sensitivity in CV and DPV measurements (Fig. 3(a) & 3(c)). This superior catalytic activity for nicotine oxidation results from the combined features of high surface area, electrical conductivity, and effective electron transfer of CNT and the layered, porous structure of *g*-C_3N_4, which is rich in nitrogen, promotes strong analyte adsorption and π-π interactions with nicotine. This is evident as an anodic peak at 0.32 V in *g*-C_3N_4/CNT/GCE CV graph. The other advantage of the association is that C_3N_4 helps prevent CNT aggregation, while CNT prevents C_3N_4 leaching. The CNT penetrate through the layers of C_3N_4, and covalent bonding enhances the overall stability and performance of the composite.

The interfacial properties and charge transfer dynamics at the *g*-C_3N_4/CNT/GCE nicotine interface were studied using EIS. The tests were conducted between 10 Hz and 1 MHz. By analysing the Nyquist plot

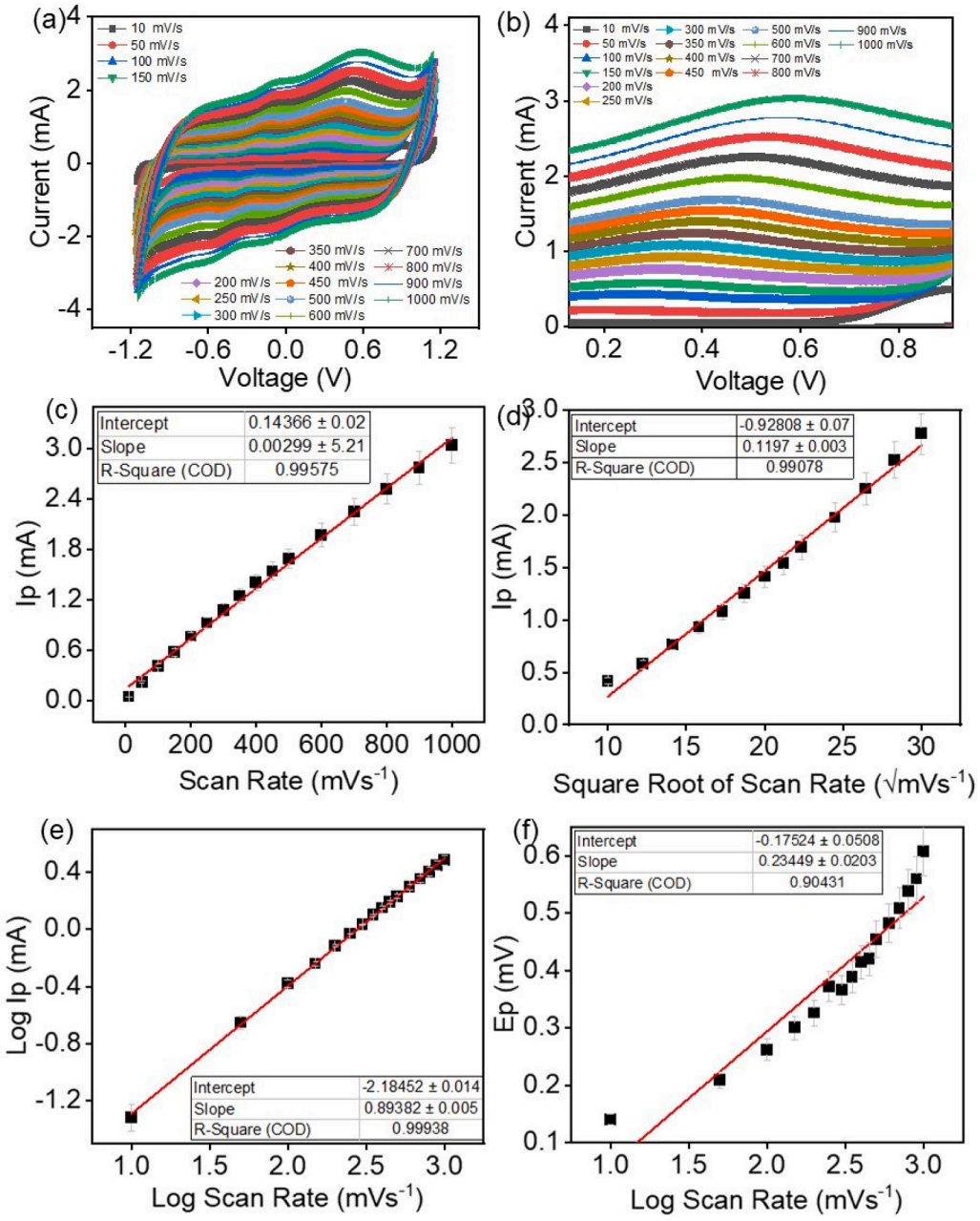

Fig. 5. (a) CV ranging from 10 mVs^{-1} to 1000 mVs^{-1} (−1.15 V to 1.15 V), 10 mM nicotine in 0.1 M PBS at pH 7. (b) Zoomed-in image of the oxidation peaks from the CV. (c) I_p(mA) *vs.* ν (mVs^{-1}). (d) Plot of I_p(mA) *vs.* $\sqrt{\nu}$ ($\sqrt{mVs^{-1}}$). (e) Plot of log(I_p) *vs.* log(ν). (f) Plot E_p (mV) *vs.* log(ν).

shown in Fig. 3(d), a very small semicircular region at the high-frequency end suggests fast and efficient electron transfer at the electrode surface, followed by a linear region (Warburg impedance), indicating diffusion-controlled processes related to the transport of nicotine molecules at lower frequencies [43,44]. The solution resistance in 100 mM nicotine is 0.34584 Ω for CNT/GCE, 0.71167 Ω for *g*-C_3N_4/CNT/GCE, and 0.76236 Ω for bare/GCE. The resistance is negligible, and the Nyquist plot indicates that the *g*-C_3N_4/CNT/GCE is a good candidate for nicotine detection. EIS Fitting of 100 mM Nicotine on *g*-C_3N_4/CNT/GCE and Equivalent circuit is shown in **Figs. S4 and S5** [45].

3.4. *Effect of pH*

The electrochemical activity of *g*-C_3N_4/CNT/GCE was studied across a pH range of 2 to 9 with a nicotine of 100 mM in 0.1 M PBS. The resulting CV (50 mVs^{-1}, −1.15 V to 1.15 V) data shown in Fig. 4(a) indicate that as the pH increases from acidic to alkaline, the oxidation peak current (I_p) and peak potential (E_p) shift negatively, suggesting the role of protons in the redox reaction is shown in the Fig. 4(b) and 4(c)

The scientific relation between the electron-proton transfer, pH and the peak potential expressed by the Nernst equation (Eq. (2)).

$$Ep = E^0 + \frac{0.0591}{n}\log\left[\frac{(OX)^a}{(R)^b}\right] - \left(\frac{0.0591m}{n}\right)pH \quad (2)$$

Where n and m are the number of electrons and protons involved in the reaction, and a and b are oxidant and reductant coefficients [46]. According to the Nernst equation, the expected slope of the E_p *vs.* pH (Figs. 4(c) and 4(d)) plot should be approximately −59 mV/pH, indicating equal involvement of protons and electrons in the electrochemical oxidation of nicotine. Any deviation from −59 mV/pH suggests either different ratios of participation by protons and electrons

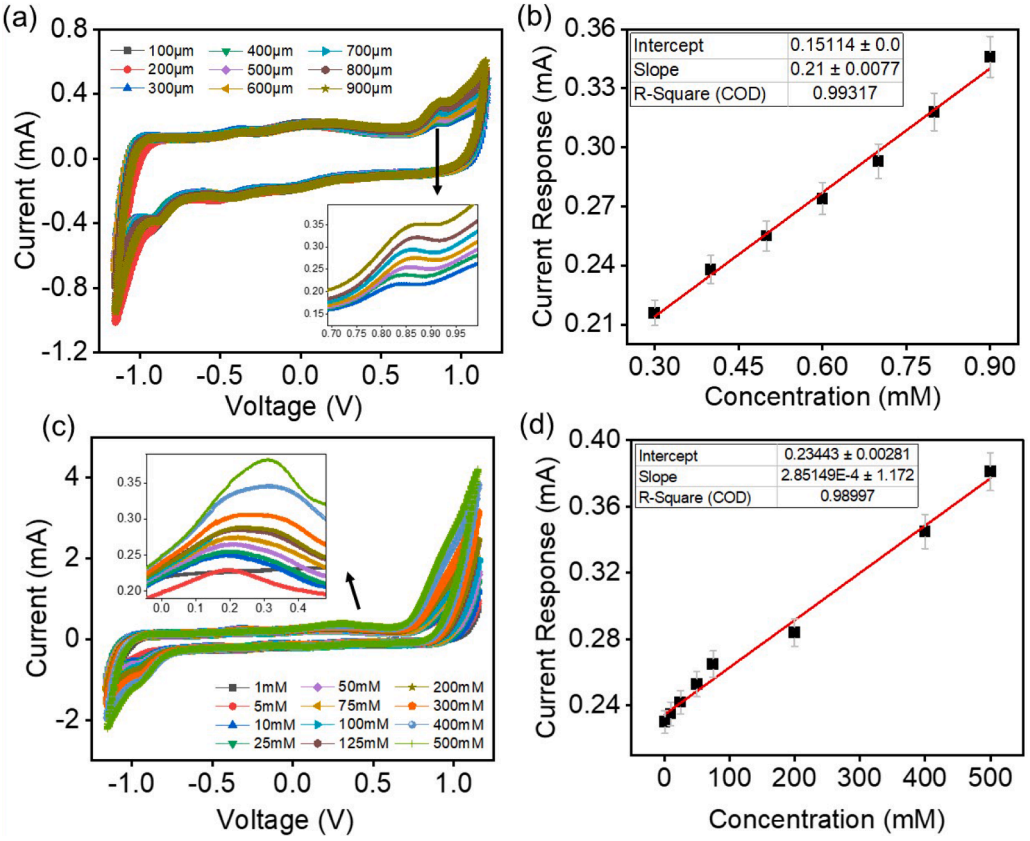

Fig. 6. (a) CV (50 mVs^{-1}, from −1.15 V to 1.15 V) of lower nicotine concentrations, ranging from 0.1 mM to 0.9 mM in 0.1 M PBS (pH 7). (b) Plot of I_p *vs.* concentration for lower nicotine concentrations. (c) CV (50 mVs^{-1}, from −1.15 V to 1.15 V) of higher nicotine concentrations, ranging from 1 mM to 500 mM in 0.1 M PBS (pH 7). (d) Plot of I_p *vs.* concentration for higher nicotine concentrations.

or more complex mechanisms. The full-range pH plot does not exhibit good linearity (R^2 = 0.69859), indicating distinct mechanisms in different pH zones. By splitting the plot into two linear ranges, each slope can be compared to the Nernst equation separately.

The acidic pH range (2–6) (Fig. 4(b)) had a slope of −74.57 mV/pH, with a linearity of R^2 = 0.84836 (Eq. (3)). This suggests that additional proton-coupled processes occur, likely due to the protonation of the pyrrolidine nitrogen in nicotine, which alters its structure and decreases its oxidation tendency. In contrast, the basic pH range (7–9) (Fig. 4(c)) had a slope of −33.08 mV/pH, with a linearity of R^2 = 0.93083 (Eq. (4)). This indicates reduced proton involvement, consistent with the deprotonated form of nicotine being more readily oxidised. This finding is evident in the current response to pH, which shows a negative shift with increasing pH, as illustrated in Fig. 4(d).

$$y = -0.0746x + 0.5591 \quad (3)$$

$$y = -0.0331x + 0.427 \quad (4)$$

This behaviour is advantageous for sensor applications, enhancing comparably more signal stability across varying pH environments and making the system more robust for real sample analysis [28].

To determine the optimal pH for further studies, we found that pH 2 gave the highest oxidation current. But at pH 7, the sensor exhibited distinct changes; the I_P was at 0.2139 mA, and the E_P was at 0.2047 V, providing a clear oxidation peak signal in a decreasing trend (Fig. 4(d)). At very low pH (2 or 3), the *g*-C_3N_4/CNT surface risks proton corrosion or damage, leading to unstable signal responses over time and poor resolution in detecting nicotine. Operating at pH 7 ensures the chemical and surface stability of the electrode, avoiding corrosion seen in strong acidic conditions and degradation in basic conditions. This enhances long-term reproducibility and improves compatibility with real samples without extensive pH adjustments, facilitating reliable nicotine detection. Most commercial vape liquids (e-liquids) have a pH around 6.0 to 8.0 and operating at pH 7 minimises the risk of degradation from flavours and additives, which may interfere with detection at extreme pH levels (2 or 9). Therefore, pH 7 was selected as the optimal working condition, balancing high current response, sharp peak definition, electrode stability, and compatibility with real sample matrices.

3.5. Scan rate study

The scan rate determines how quickly the applied potential is swept during an electrochemical experiment, helping to study the interaction between the analyte and the electrode surface. In this study, 10 mM nicotine in 0.1 M PBS at pH 7 was analysed using scan rates ranging from 10 mVs^{-1} to 1000 mVs^{-1} from −1.15 V to 1.15 V to evaluate its electrochemical behaviour on the *g*-C_3N_4/CNT/GCE (Fig. 5(a)). Distinct oxidation and reduction peaks were observed, with a slight positive shift in peak potential as the scan rate increased, indicating a quasi-reversible system (Fig. 5(b)). The CV shows that peak current increased noticeably with scan rate, as faster potential sweeps reduce the diffusion layer thickness, allowing more nicotine to reach the electrode surface rapidly, resulting in higher current, a characteristic of diffusion-controlled behaviour [47]. A strong linear correlation (R^2 = 0.99575) between scan rate (ν, mV/s) and anodic peak current (Ip, mA), following Eq. (5), suggests an adsorption-controlled process (Fig. 5(c)).

$$Ip(mA) = 0.0003 \times \nu(mVs^{-1}) + 0.1437 \quad (5)$$

Similarly, a linear relationship (R^2 = 0.99078) between I_p and the square root of the scan rate ($\nu^{1/2}$), following Eq. (6), indicates the involvement of diffusion-controlled behaviour as well (Fig. 5(d)).

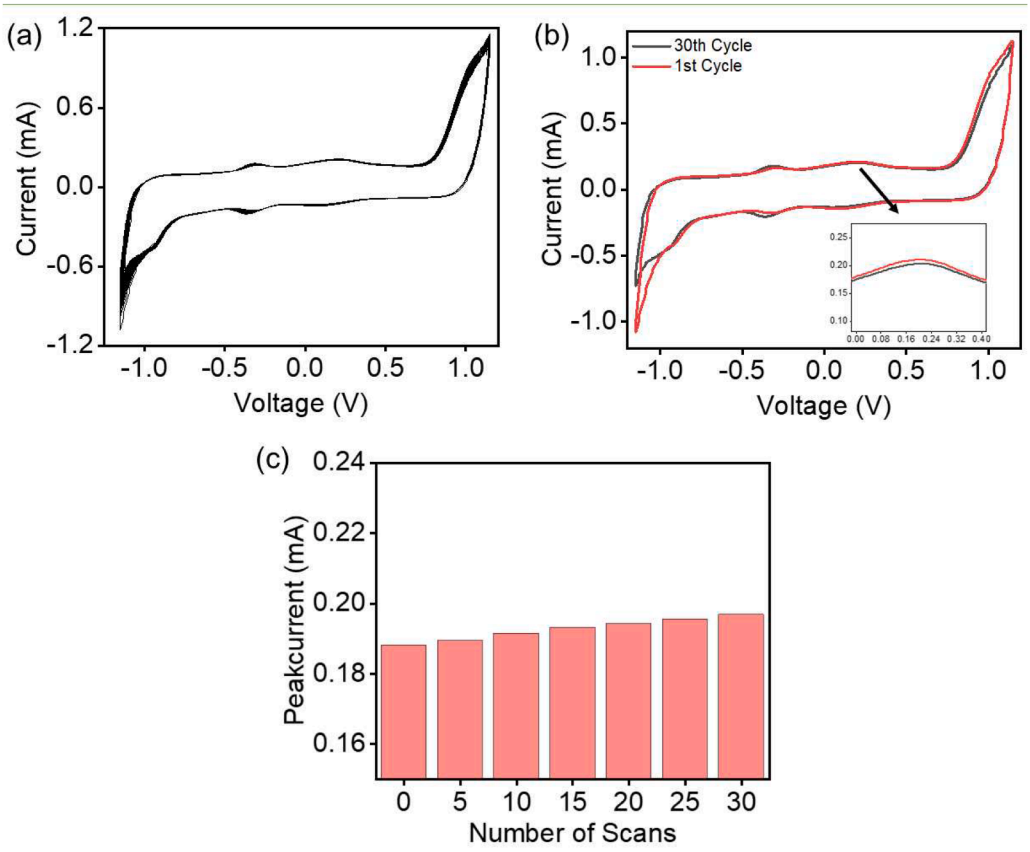

Fig. 7. (a) 30 consecutive CV scans (50 mVs^{-1}, −1.15 V to 1.15 V) in 10 mM nicotine solution in 0.1 M PBS. (b) CV of 1st and 30th cycle. (c) Comparison of I_p (mA) *vs.* number of scans.

$$Ip(mA) = 0.1197 \times \nu^{1/2}\left((mVs^{-1})^{1/2}\right) - 0.9281 \quad (6)$$

These findings suggest a mixed control mechanism involving nicotine oxidation at the *g*-C_3N_4/CNT/GCE surface. To further confirm this, a plot of log I_p *versus* log ν showed linearity ($R^2 = 0.99938$) with a slope of 0.894 (Eq. (7)), which lies between 0.5 (diffusion control) and 1.0 (adsorption control), reinforcing the mixed-controlled nature of the process (Fig. 5(e)).

$$\text{Log } I_p \text{ (mA)} = (0.8938 * \log \nu \text{ (mV)}) - 2.1845 \quad (7)$$

This means some nicotine molecules diffuse from the solution to the electrode surface, while others are adsorbed onto the surface and undergo oxidation. The E_p also showed a linear correlation ($R^2 = 0.90431$) with the logarithm of the scan rate, represented by Eq. (8), following Laviron's model, as shown in Eq. (9) (Fig. 5(f)).

$$Ep(mV) = (0.2345 * \log \nu \text{ (mV)}) + 0.1752 \quad (8)$$

This confirms the quasi-reversible nature of the electron transfer, allowing for the calculation of the number of electrons (n) involved in the process.

$$Ep = E^0 + \left(\frac{RT}{\alpha nF}\right)\ln\left(\frac{RTk^o}{\alpha nF}\right) - \left(\frac{RT}{n\alpha nF}\right) In\ \nu \quad (9)$$

Where n is the number of electrons transferred, E^0 is the formal redox potential, α is the charge transfer coefficient, R is the universal gas constant, T is the temperature, k^0 is the standard heterogeneous constant (3.63 cm^{-1}), and F is the Faraday constant [35]. The nicotine oxidation is a quasi-reversible process, and the charge transfer coefficient was assumed to be 0.5. As a result, the number of electrons (n) was calculated to be 0.504, which is approximately 1, indicating that the process involves the transfer of a single electron.

3.6. Calibration study

To identify the calibration curve, limit of detection (LOD), and limit of quantitation (LOQ), CV (50 mVs^{-1}, −1.15 V to 1.15 V) was recorded with different nicotine concentrations ranging from 0.1 mM to 500 mM in 0.1 M PBS (pH 7), Fig. 6(a) and 6(c). The peak current is plotted against nicotine concentrations, and the calibration curve showed two separate linear regions (Fig. 6(b) and 6(d)). At low nicotine concentrations, the *g*-C_3N_4/CNT surface provides many free active sites, allowing nicotine molecules to adsorb more effectively, which leads to a higher R^2 value. In this region, the oxidation peak appeared at 0.854 mV with a correlation coefficient of 0.99317, described by Eq. (10).

$$Ip(mA) = 0.21 * \text{Nicotine concentration (mM)} + 0.1511 \quad (10)$$

At higher concentrations, many of these sites become occupied, and the process is limited by the diffusion of nicotine from the solution to the electrode surface. This produces a second linear range with lower sensitivity. In this region, the oxidation peak was observed at 0.3240 mV with a correlation coefficient of 0.98997, as expressed in Eq. (11).

$$Ip(mA) = 0.0003 * \text{Nicotine concentration (mM)} + 0.2344 \quad (11)$$

At high concentrations, the oxidation peak potential also shifted to less positive values, which may be attributed to increased resistance effects and changes in the electron transfer process when the surface is heavily covered. For the calculation of LOD and LOQ, the low-concentration range was used, as it showed a stronger and more reliable response. The standard deviation and slope from the low-concentration data were used, as outlined in Eqs. (12) and 13.

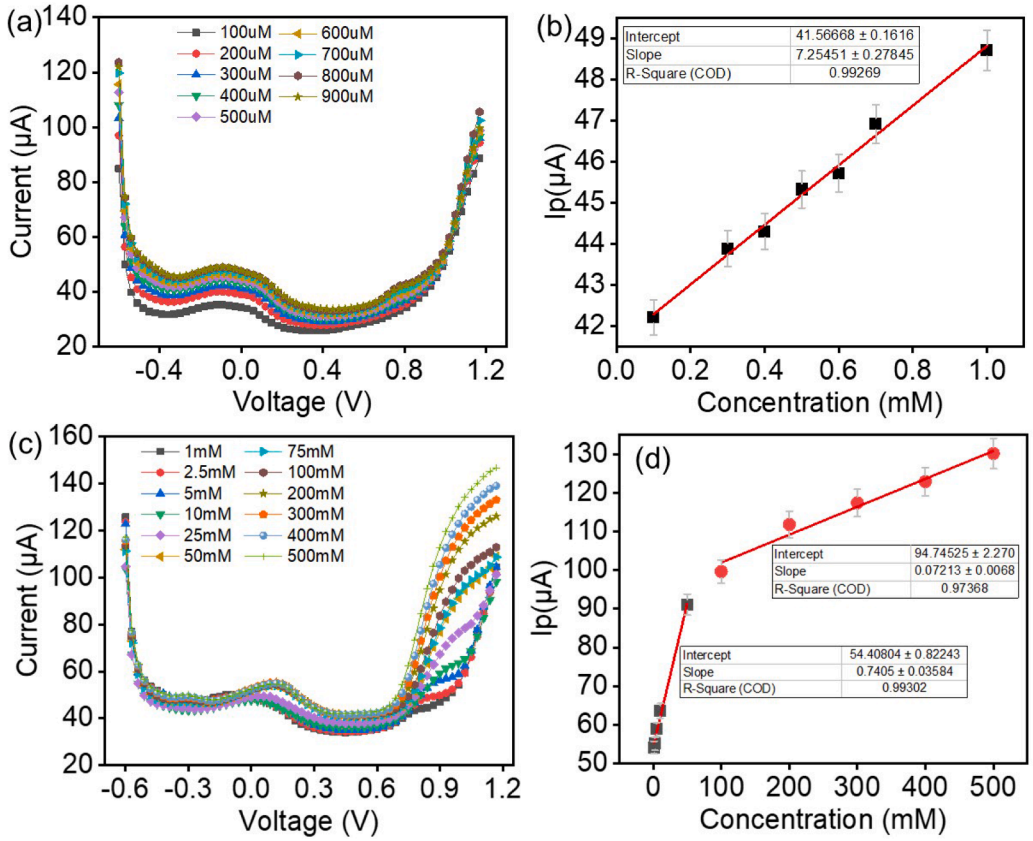

Fig. 8. (a) DPV of lower nicotine concentrations, ranging from 0.1 mM to 0.9 mM in 0.1 M PBS (pH 7). (b) Plot of I_p *vs.* concentration for lower nicotine concentrations. (c) DPV of higher nicotine concentrations, ranging from 1 mM to 500 mM in 0.1 M PBS (pH 7). (d) Plot of I_p *vs.* concentration for higher nicotine concentrations.

$$\text{LOD} = 3.3\left|\frac{\sigma}{s}\right| \tag{12}$$

$$\text{LOQ} = 10\left|\frac{\sigma}{s}\right| \tag{13}$$

where σ is the standard deviation (SD) and s is the slope of peak current *versus* nicotine concentrations [46]. To calculate the LOD and LOQ, the standard deviation and slope were taken from the lower concentration. The LOD was found to be 0.0773 mM and the LOQ was 0.2343 mM.

3.7. Repeatability and stability

To understand the electrochemical stability and repeatability of the *g*-C_3N_4/CNT/GCE, 30 consecutive CV scans (50 mVs^{-1}) were performed in a 10 mM nicotine solution in 0.1 M PBS (Fig. 7(a)). While analysing the 1st and 30th scans, the E_p remained unchanged, and a comparatively slight downward shift in I_p was observed in the 30th scan (Fig. 7(b)). This shift can be attributed to the reduced availability of active sites resulting from repeated redox cycling. The retention can be calculated using Eq. (14), as shown below.

$$\text{Retention} = \left(\frac{I^{30th}}{I^{1st}}\right) * 100 \tag{14}$$

The calculated retention is 96.36 %, confirming that the sensor exhibits good electrochemical operational stability for repeated nicotine detection despite minimal signal attenuation.

4. Application

4.1. Electrochemical performance and calibration study using Anapot

The active surface area of the screen-printed electrode was measured using CV at scan rates ranging from 10 to 300 mV s^{-1} **(Fig. S6(a))**. A 5 mM solution of $K_3[Fe(CN)_6]$ in 0.1 M KCl was used as the test solution, as described in Section 3.2. The comparison of the CVs at a scan rate of 50 mVs^{-1} revealed that the *g*-C_3N_4/CNT-coated screen-printed electrode exhibited a significantly larger active surface area than the bare screen-printed electrode **(Fig. S6(b))**. Using the Randles–Ševčík equation (Eq. (1)), the surface area of the modified screen-printed electrode was found to be approximately 0.003 cm^2, while the *g*-C_3N_4/CNT-coated screen-printed electrode had a surface area of 0.054 cm^2. This indicates that the addition of *g*-C_3N_4/CNT greatly enhances the electrochemical properties of the electrode.

To identify the calibration curve, limit of detection (LOD), and limit of quantitation (LOQ), differential pulse voltammetry (DPV) was performed with nicotine concentrations ranging from 0.1 mM to 500 mM in 0.1 M PBS (pH 7), Fig. 8(a) and 8(c). The peak current (Ip, μA) was plotted against nicotine concentrations (mM) for both lower and higher concentration ranges, as shown in Fig. 8(b) and 8(d). For the lower concentration range (0.1 mM to 0.9 mM), an oxidation peak appeared at 0.92 mV, with a linear correlation coefficient of 0.99269, described by Eq. (15).

$$\text{Ip}(\mu\text{A}) = 7.2545 * \text{Nicotine concentration (mM)} + 41.567 \tag{15}$$

For the higher concentration range, two linear trends were observed: one is from 1 mM to 75 mM and another from 100 mM to 500 mM at 0.97 mV. The oxidation peak for the first trend has a linearity of 0.99302 (Eq. (16)), while the second trend has a linearity of 0.97368 (Eq. (17)).

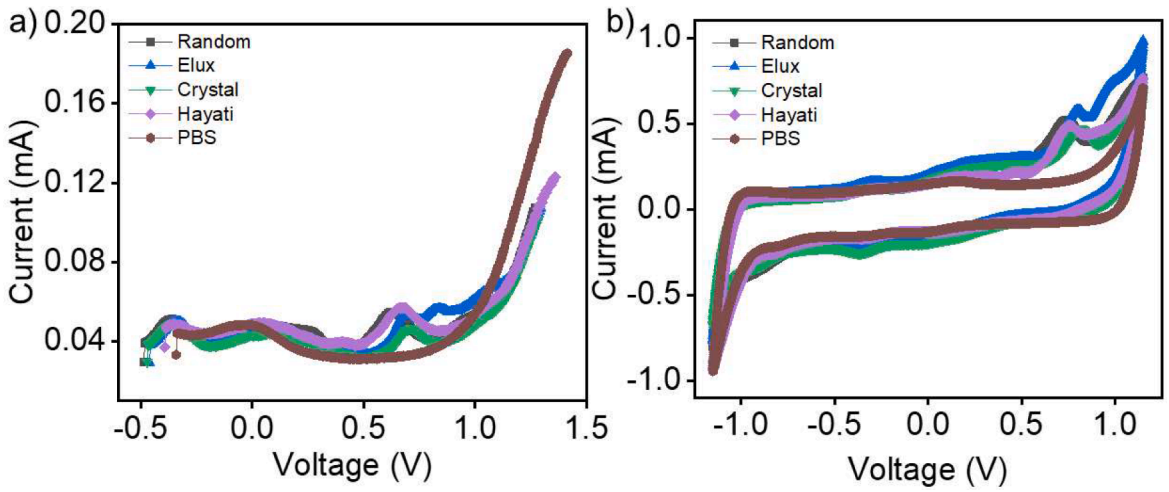

Fig. 9. Voltametric response of commercial vape samples (pH 7), (a) DPV response, (b) CV Response.

Table 2
Expected and resulted concentration of commercial vape samples.

Sample Name	Expected Concentration (mM)	Resulted Concentration (mM)
Random tornado	123.3	109
Elux legends	123.3	176.3333333
Ske crystal	61.7	69.53333333
Hayati pro max	0	−144.3333333
0.1 M PBS	0	−298.1333333

The process is recorded and shown in supporting information **Video V1.**

$$Ip(\mu A) = (0.7405 * \text{Nicotine concentration (mM)}) + 54.408 \quad (16)$$

$$Ip(\mu A) = (0.0721 * \text{Nicotine concentration (mM)}) + 94.745 \quad (17)$$

The three linear regions observed in Fig. 8 likely result from changes in the rate limiting process as the nicotine concentration increases. At low concentrations, the electrode surface has many free, high-affinity active sites, so adsorption dominates the response, producing a steep slope and high linearity ($R^2 = 0.99269$). In the middle-concentration range, partial site occupation and heterogeneity of active sites lead to mixed control, where both adsorption and diffusion contribute, maintaining the linearity ($R^2 = 0.99302$). At high concentrations, most active sites are occupied, and the process becomes diffusion-limited, further influenced by surface coverage, increased solution resistance, and changes in electron-transfer kinetics, resulting in a third linear region with lower sensitivity (R^2 = 97,368). Using the formulas for LOD and LOQ, the standard deviation and slope were taken from the lower concentration range. The LOD was determined to be 0.0735 mM, and the LOQ was 0.2229 mM. The results from various literature are summarised in **Table S1**, which compares the specifications of the current study regarding materials, methods, limits of detection (LOD), and linearity with those of previously published approaches.

4.2. Selectivity and real sample analysis

To understand the selectivity of the g-C_3N_4/CNT/GCE sensor, we conducted real-time testing using commercial vape samples. The CV and DPV results of the vape samples at pH 7 are demonstrated in Fig. 9(a) and 9(b). While analysing the CV, multiple oxidation peaks were observed, which is expected due to the presence of alcohols and flavouring compounds. Among these, one of the peaks around 0.32 V is consistent with the oxidation peak identified in the standard nicotine concentration study. This correlation strongly suggests that the observed peak corresponds to the nicotine oxidation peak; the resulting concentration is provided in Table 2. According to the results, the expected 0 % nicotine samples yield negative values, and the vape sample from Ske has a lower concentration of 109 mM instead of the 123.3 mM that is labelled. The vape sample from Elux has a nicotine content that is relatively high at 176.3 mM, which is more than what is displayed on the label and exceeds the legal standard of 123.3 mM (20 mg/mL).

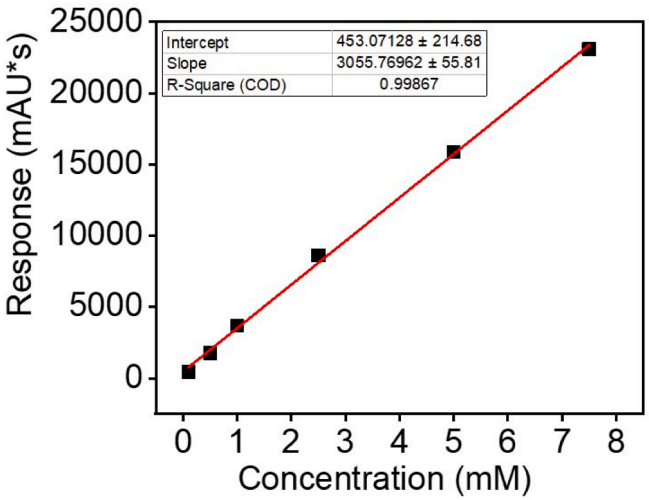

Fig. 10. Mean standard HPLC calibration curve of nicotine showing linearity over a concentration range of 0.1–7.5 mM.

Table 3
Expected and resulted concentration of commercial vape samples using HPLC.

Company name	Flavour	Nicotine percentage	Batch number	Expiry Date	Nicotine dose per puff
Random tornado	Blueberry cherry cranberry	20 mg/ml, 2 %	—-	—-	66 µg
Elux legends	Grape	20 mg/ml, 2 %	KA20240315NJ	07/04/2026	133 µg
Ske crystal	Triple mango	10 mg/ml, 1 %	CRYTM 10–003	31/01/2027	110 µg
Hayati pro max	Triple mango	0 %	37EA23C	23/10/2026	0 µg

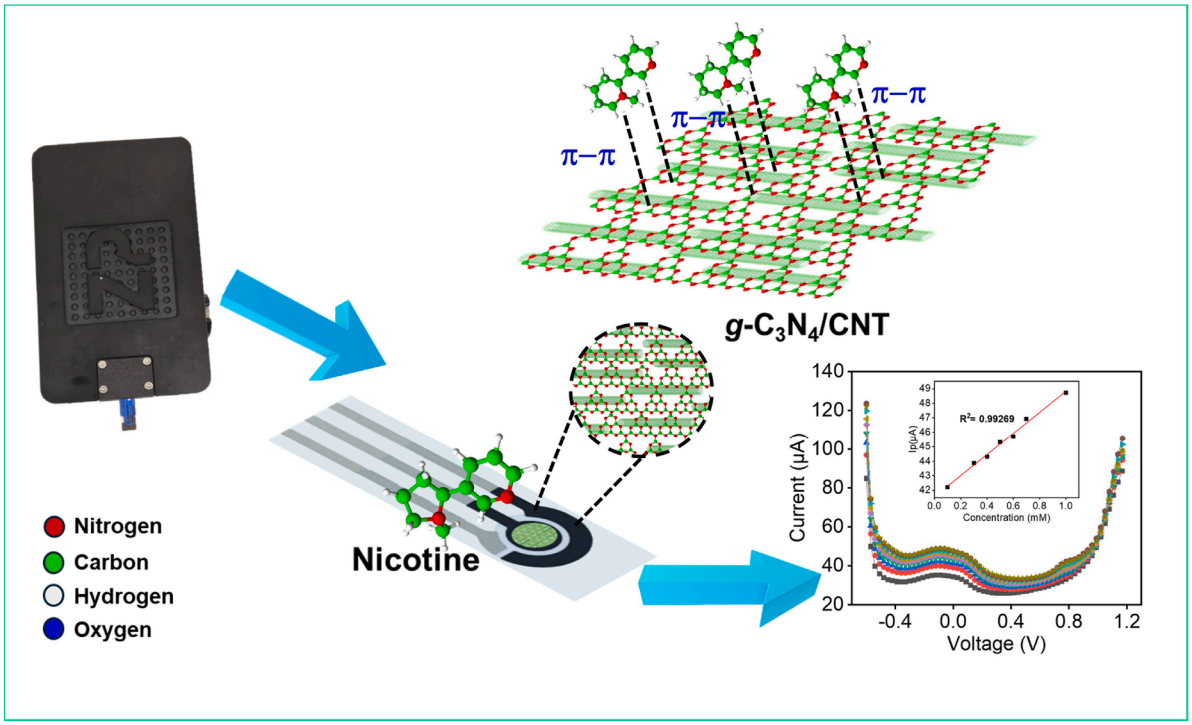

Fig. 11. Plausible mechanistic overview of the nicotine sensing process on the surface of *g*-C_3N_4/CNT.

4.3. Validation using HPLC

The sensor's reliability was validated using HPLC, a traditional and trusted method for quantifying nicotine in vape samples. The method's linearity was validated over a nicotine concentration range of 0.1–7.5 mM, with an R^2 value of 0.99867 with Eq. (18), shown in Fig. 10.

$$\text{Response} = (3059.6 * \text{Nicotine Concentration(mM)}) + 339.94 \quad (18)$$

The resulting HPLC results were tabulated in Table 3. The conclusions were nearly identical when comparing both sensors and HPLC results of vape samples, confirming the sensor's selectivity and applicability for detecting real samples.

5. Sensing mechanism

g-C_3N_4 is a 2D layered, nitrogen-rich, π-conjugated polymer known for its excellent electron-donating ability. Its π–π stacking interactions with aromatic compounds like nicotine enhance adsorption (Fig. 11), while exposed nitrogen sites form hydrogen bonds with nicotine's nitrogen atoms, as shown in the FTIR and XRD results (Fig. 1(a) and 1(d)). The material's high surface area, resulting from its porous structure, enhances nicotine adsorption; however, its semi conductivity can hinder electron transport [48]. To address this, CNTs are incorporated. CNTs provide high surface area, excellent electrical conductivity, and fast charge transport pathways, acting as conductive bridges between *g*-C_3N_4 layers and the electrode as observed in the SEM images (Fig. 1(b)) [49]. They enhance the electrochemical response and promote faster electron transfer kinetics at the electrode-electrolyte interface, effectively shuttling electrons from oxidised nicotine to the electrode. The ratio of *g*-C_3N_4 to CNT is crucial; excessive CNT can hinder nicotine absorption despite facilitating rapid electron transfer. Through careful consideration and experimentation, the ratio of 90:10 (*g*-C_3N_4: CNT) is established. The binder, chitosan (2 % in acetic acid), forms a biocompatible, porous film that enhances mechanical stability. Its amine (-NH_2) and hydroxyl (-OH) groups aid in nicotine adsorption through hydrogen bonding without blocking electron transfer. Chitosan creates a semi-permeable film that allows selective diffusion of nicotine while minimising interference [50].

Nicotine molecules diffuse toward the electrode and interact with active surface sites via non-covalent forces. Adsorbed molecules undergo a quasi-reversible, single-electron oxidation, with electrons transferred through *g*-C_3N_4/CNTs and ultimately to the electrode. This oxidation primarily occurs at the pyrrolidine nitrogen, which is more basic and readily oxidised than the pyridine nitrogen. Nicotine adsorbs onto the *g*-C_3N_4/CNT surface through π-π stacking and hydrogen bonding. During oxidation, the lone pair on the nitrogen is lost, forming a radical cation, with the electron transferred to the *g*-C_3N_4 conduction band and relayed through the π-conjugated system of CNTs to the electrode, generating a linear current response proportional to nicotine concentration. This process is quasi-reversible, as the radical cation can undergo further reactions. The semiconducting properties of *g*-C_3N_4, with a bandgap of approximately 2.7 eV, facilitate electron transfer due to its favourable alignment with the highest occupied molecular orbital (HOMO) of nicotine (~−6.5 eV), and EIS shows lower resistance (Rs), indicating fast electron shuttling [35,51]. The oxidation process is controlled by both diffusion from the bulk solution and surface adsorption, resulting in a mixed diffusion–adsorption-controlled system. The combination of rapid charge transport, surface interaction, and favourable energetics results in a sensitive and stable electrochemical response for nicotine detection.

6. Conclusion

This research demonstrates the development of a novel, sustainable electrochemical sensor based on a composite of *g*-C_3N_4 and CNTs for the sensitive and efficient detection of nicotine in commercial vape samples. The integration of CNTs significantly enhances the conductivity of *g*-C_3N_4, while chitosan serves as a biocompatible binder, ensuring the stability and adherence of the sensor material to GCE. The sensor exhibits remarkable selectivity and sensitivity, achieving a detection limit of 0.0773 mM and a limit of quantification of 0.2343 mM, with excellent repeatability and operational stability at room temperature. The successful validation of the sensor's performance against conventional

HPLC methods underscores its practical applicability in real-world scenarios.

The adaptation of the *g*-C_3N_4/CNT composite onto a carbon-based printed electrode for real-time applications further enhances its potential for widespread use in nicotine monitoring. The findings from this study highlight the promise of *g*-C_3N_4/CNT composites as effective and environmentally friendly sensing materials, paving the way for future developments in electrochemical sensor technology to ensure consumer product safety and public health. This work contributes to the advancement of sensor technology and emphasises the importance of sustainability in the design of analytical tools.

CRediT authorship contribution statement

Reshma Nair: Writing – original draft, Investigation, Formal analysis, Data curation. **Danielson Ngo Joseph:** Writing – original draft, Formal analysis, Data curation. **Francesco Spiedo:** Investigation, Formal analysis. **Bal Virdee:** Writing – review & editing, Supervision. **Bhaven Patel:** Writing – review & editing, Supervision, Investigation, Formal analysis. **Devagi Kanakaraju:** Writing – review & editing, Formal analysis, Data curation. **Priyanka Ganguly:** Writing – review & editing, Visualization, Validation, Supervision, Funding acquisition, Conceptualization.

Declaration of competing interest

The authors declare that they have no known competing financial interests or personal relationships that could have appeared to influence the work reported in this paper.

Acknowledgements

We acknowledge London Metropolitan University for the Vice Chancellor's Postgraduate (PGR) Scholarships (R.N.) and a Research Transformation grant. We acknowledge HPLC technician Shahrzad Nateghian and Haritha Sudha Nair at the Science Centre, London Metropolitan University, who supported the project.

Supplementary materials

Supplementary material associated with this article can be found, in the online version, at doi:10.1016/j.electacta.2025.147365.

Data availability

Data will be made available on request.

References

[1] Gov.UK, *Research and analysis - "Nicotine vaping in England: 2022 evidence update main findings"*, Available from, https://www.gov.uk/government/publications/nicotine-vaping-in-england-2022-evidence-update/nicotine-vaping-in-england-2022-evidence-update-main-findings, 2022.
[2] J. Meehan, et al., The adverse effects of vaping in young people, Glob. Pediatr. 9 (2024) 100190.
[3] D.L. Palazzolo, Electronic cigarettes and vaping: a new challenge in clinical medicine and public health. a literature review, Front. Public Health 1-2013 (2013).
[4] M. Abd-Elsabour, et al., A novel electrochemical sensor for detection of nicotine in tobacco products based on graphene oxide nanosheets conjugated with (1, 2-naphthoquinone-4-sulphonic acid) modified glassy carbon electrode, Nanomaterials 12 (14) (2022) 2354.
[5] Z. Liang, et al., A smart portable sensor with ratio and dual-mode for in situ detection of nicotine in tobacco leaves, IEEE Sens. J. 24 (1) (2024) 71–77.
[6] S. Nihal, et al., A diverse paper sensor for the rapid determination of nicotine and cotinine traces in air, vaping liquid, and human saliva, Talanta 292 (2025) 127929.
[7] Gov.UK, Guidance "E-cigarettes: regulations for consumer products", Available from: https://www.gov.uk/guidance/e-cigarettes-regulations-for-consumer-products?utm_source=chatgpt.com, 2016.
[8] Gov.UK, Drug safety update "e-cigarette use or vaping: reminder to remain vigilant for suspected adverse reactions and safety concerns and report them to the yellow card scheme", Available from: https://www.gov.uk/drug-safety-update/e-cigarette-use-or-vaping-reminder-to-remain-vigilant-for-suspected-adverse-reactions-and-safety-concerns-and-report-them-to-the-yellow-card-scheme?utm_source=chatgpt.com, 2023.
[9] HUI, S. *The UK will ban disposable vapes and curb candy-flavored e-cigarettes that attract children under 18*. January 2024.
[10] H. Farrimond, E-cigarette regulation and policy: UK vapers' perspectives, Addiction 111 (6) (2016) 1077–1083.
[11] J. Li, et al., A colorimetric sensor with dual-ratio and dual-mode for detection of nicotine in tobacco samples, Anal. Methods 15 (46) (2023) 6377–6384.
[12] C.N. Man, et al., Determination of hair nicotine by gas chromatography–mass spectrometry, J. Chromatogr. B 877 (3) (2009) 339–342.
[13] M.C. Acosta, et al., Urine cotinine as an index of smoking status in smokers during 96-hr abstinence: comparison between gas chromatography/mass spectrometry and immunoassay test strips, Nicotine Tob. Res. 6 (4) (2004) 615–620.
[14] Y. Zhou, et al., A new spectrofluorometric method for the determination of nicotine base on the inclusion interaction of methylene blue and cucurbit[7] uril, Microchim. Acta 164 (1) (2009) 63–68.
[15] M. Page-Sharp, et al., Measurement of nicotine and cotinine in human milk by high-performance liquid chromatography with ultraviolet absorbance detection, J Chromatogr. B Anal. Technol. Biomed. Life Sci. 796 (1) (2003) 173–180.
[16] A.W. Abu-Qare, M.B. Abou-Donia, Quantification of nicotine, chlorpyrifos and their metabolites in rat plasma and urine using high-performance liquid chromatography, J. Chromatogr. B: Biomed. Sci. Appl. 757 (2) (2001) 295–300.
[17] A. Alhusban, S. Ata, Simple HPLC method for rapid quantification of nicotine content in e-cigarettes liquids, Acta Chromatogr. (2020).
[18] E.C. Figueiredo, et al., On-line molecularly imprinted solid-phase extraction for the selective spectrophotometric determination of nicotine in the urine of smokers, Anal. Chim. Acta 635 (1) (2009) 102–107.
[19] J.J. Langone, H.B. Gjika, H. Van Vunakis, Nicotine and its metabolites. Radioimmunoassays for nicotine and cotinine, Biochemistry 12 (24) (1973) 5025–5030.
[20] G.D. Byrd, R.A. Davis, M.W. Ogden, *A rapid LC-MS-MS method for the determination of nicotine and cotinine in serum and saliva samples from smokers*: v*alidation and comparison with a radioimmunoassay method*, J. Chromatogr. Sci. 43 (3) (2005) 133–140.
[21] K. Mitsubayashi, et al., Bioelectronic sniffer for nicotine using enzyme inhibition, Anal. Chim. Acta 573-574 (2006) 69–74.
[22] M.S. Lin, J.S. Wang, C.H. Lai, Electrochemiluminescent determination of nicotine based on tri(2,2′-bipyridyl) ruthenium (II) complex through flow injection analysis, Electrochim. Acta 53 (26) (2008) 7775–7780.
[23] A.A.M. Stolker, et al., Determination of nicotine and cotinine in rat plasma by liquid chromatography–tandem mass spectrometry, J. Chromatogr. A 1020 (1) (2003) 35–43.
[24] A. Marsh, B.J. Clark, K.D. Altria, Orthogonal separations of nicotine and nicotine-related alkaloids by various capillary electrophoretic modes, Electrophoresis 25 (9) (2004) 1270–1278.
[25] M. Kowalcze, M. Jakubowska, Voltammetric determination of nicotine in electronic cigarette liquids using a Boron-Doped Diamond Electrode (BDDE), Diam. Relat. Mater 103 (2020) 107710.
[26] A. Karthika, et al., Electrochemical sensing of nicotine using CuWO(4) decorated reduced graphene oxide immobilized glassy carbon electrode, Ultrason. Sonochem. 55 (2019) 196–206.
[27] A. Dayan, et al., 3d-printed electrochemical sensor for rapid nicotine detection in e-cigarettes and sweat. Available At SSRN 5225231, 2025.
[28] A.G.d.S. Neto, et al., *Electrochemical sensor based on tadpole-shaped Au nanostructures supported on* TiO2: enh*anced detection of nicotine in electronic cigarettes and clinical samples*, Talanta 287 (2025) 127652.
[29] S.C. Pillai, P. Ganguly, 2D nanomaterials and composites for energy storage and conversion, 2D Mater. Energy Storage Convers. (2021).
[30] D.K. Neethipathi, et al., Electrochemical detection of Fe2+ ions in water using 2-dimensional g-C3N4 modified glassy carbon electrode-based sensor, in: 2023 IEEE Applied Sensing Conference (APSCON), 2023.
[31] S. Panneri, et al., Photoregenerable, bifunctional granules of carbon-doped g-C3N4 as adsorptive photocatalyst for the efficient removal of tetracycline antibiotic, ACS Sustain. Chem. Eng. 5 (2) (2017) 1610–1618.
[32] G. Priyanka, Sensors for water quality assessment in extreme environmental conditions. Sensing Technologies for Real Time Monitoring of Water Quality, IEEE, 2023, pp. 253–282.
[33] M.A. Khan, et al., *Recent advances over the doped g-C3N4 in photocatalysis*: a r*eview*, Coord. Chem. Rev. 522 (2025) 216227.
[34] J. Wang, S. Wang, *A critical review on graphitic carbon nitride (g-C3N4)-based mater*ials: preparat*ion, modification and environmental application*, Coord. Chem. Rev. 453 (2022) 214338.
[35] S. Madasu, et al., Graphitic carbon nitride (g–C3N4)-based electrochemical sensors for the determination of antiviral drug acyclovir, Mater. Chem. Phys. 312 (2024) 128650.
[36] Y.M. Shanbhag, et al., Direct and sensitive electrochemical evaluation of pramipexole using Graphitic Carbon Nitride (GCN) Sensor, Biosens 12 (8) (2022) 552.
[37] D.K. Neethipathi, et al., MoS2 modified screen printed carbon electrode based flexible sensor for detection of copper, in: 2022 IEEE International Conference on Flexible and Printable Sensors and Systems (FLEPS), 2022.
[38] A.K. Aliyana, et al., Disposable pH sensor on paper using screen-printed graphene-carbon ink modified zinc oxide nanoparticles, IEEE Sens. J. 22 (21) (2022) 21049–21056.

[39] A. Nasri, et al., Sensing properties of g-C3N4/Au nanocomposite for organic vapor detection, Biosens 13 (3) (2023) 315.
[40] N.L. Lukman Hekiem, et al., Effect of chitosan dissolved in different acetic acid concentration towards VOC sensing performance of quartz crystal microbalance overlay with chitosan, Mater. Lett. 291 (2021) 129524.
[41] C. Cheng, et al., Hierarchical all-carbon nanozyme architectures for enhanced intelligent rutin detection, Chem. Eng. J. 514 (2025) 163289.
[42] M.M. Shanbhag, et al., Cholesterol intercalated 2D graphene oxide sheets fabricated sensor for voltammetric analysis of theophylline, FlatChem 28 (2021) 100255.
[43] M. Prince, et al., 2D metal-organic framework Cu3(HHTP)2 composite electrode for flexible energy storage applications, J. Power Sources 631 (2025) 236214.
[44] F. Paul, et al., RF-sputtered Al-doped ZnO-based transparent electrochemical capacitors developed as a structural energy storage to replace double-glazed window for a smart building, Appl. Phys. Lett. 126 (13) (2025).
[45] R. Nair, et al., Electrochemical energy storing performances of printed LaFeO3 coated with PEDOT: PSS for hybrid supercapacitors, Chem. Eng. J. 504 (2025) 158781.
[46] J. Rajendran, A.N. Reshetilov, A.K. Sundramoorthy, An electrochemically exfoliated graphene/poly(3,4-ethylenedioxythiophene) nanocomposite-based electrochemical sensor for the detection of nicotine, Mater. Adv. 2 (10) (2021) 3336–3345.
[47] P. Ganguly, et al., Influence of thickness of screen printed carbon electrodes on electrochemical sensing, in: 2022 IEEE International Conference on Flexible and Printable Sensors and Systems (FLEPS), 2022.
[48] A. Idris, et al., *Graphitic* carbon nitride: a hi*ghly electroactive nanomaterial for environmental and clinical sensing*, Sensors 20 (2020) 5743.
[49] A.-M. Nasture, et al., Water quality carbon nanotube-based sensors technological barriers and late research trends: a bibliometric analysis, Chemosensors 10 (5) (2022) 161.
[50] S. Chauhan, A. Thakur, Chitosan-based biosensors-a comprehensive review, in: Materials Today: Proceedings, 2023.
[51] S. Dheivamalar, L. Sugi, K. Ambigai, Density functional theory study of exohedral carbon atoms effect on electrophilicity of nicotine: comparative analysis, Comput. Chem. 4 (1) (2016) 17–31.